**7530** *Inorg. Chem.* **2010**, *49*, 7530–7535
DOI: 10.1021/ic101014g

Inorganic Chemistry
Article

# Oxo- and Hydroxomanganese(IV) Adducts: A Comparative Spectroscopic and Computational Study

**Swarup Chattopadhyay,[†] Robert A. Geiger,[†] Guochuan Yin,[‡] Daryle H. Busch,[†] and Timothy A. Jackson*,[†]**

[†]*Department of Chemistry and Center for Environmentally Beneficial Catalysis, University of Kansas, 1251 Wescoe Hall Drive, Lawrence, Kansas 66045, and* [‡]*School of Chemistry and Chemical Engineering, Huazhong University of Science and Technology, Wuhan 430074, China*

Received May 24, 2010

The electronic structures of the bis(hydroxo)manganese(IV) and oxohydroxomanganese(IV) complexes $[Mn^{IV}(OH)_2(Me_2EBC)]^{2+}$ and $[Mn^{IV}(O)(OH)(Me_2EBC)]^{+}$ were probed using electronic absorption, magnetic circular dichroism (MCD), and variable-temperature, variable-field MCD spectroscopies. The d−d transitions of $[Mn^{IV}(OH)_2(Me_2EBC)]^{2+}$ were assigned using a group theory analysis coupled with the results of time-dependent density functional theory computations. These assignments permit the development of an experimentally validated description for the $\pi$ and $\sigma$ interactions in this complex. A similar analysis performed for $[Mn^{IV}(O)(OH)(Me_2EBC)]^{+}$ reveals that there is a significant increase in the ligand character in the Mn $\pi^*$ orbitals for the $Mn^{IV}{=}O$ complex relative to the bis(hydroxo)manganese(IV) complex, whereas the compositions of the Mn $\sigma^*$ orbitals are less affected. Because of the steric features of the $Me_2EBC$ ligand, we propose that H-atom transfer by these reagents proceeds via the $\sigma^*$ orbitals, which, because of their similar compositions among these two compounds, leads to modest rate enhancements for the $Mn^{IV}{=}O$ versus $Mn^{IV}OH$ species.

## Introduction

The oxygenation of organic substrates by transition-metal centers is of fundamental importance in biological and synthetic transformations. For example, Fe and Mn centers supported by a variety of ligands can mediate the oxidation of C−H, N−H, or O−H bonds.[1−4] In most cases, high-valent oxometal species (i.e., $Fe^{V/IV}{=}O$ and $Mn^{V/IV}{=}O$ adducts) are commonly presumed as active oxidants.[5−9] Middle- to high-valent hydroxometal adducts can also take part in H-atom-transfer (HAT) and oxygenation reactions,[10−15] with iron and manganese lipoxygenase enzymes serving as key examples.[16−18] Much current effort is focused on comparing the properties of oxo- and hydroxometal species to understand their reactivities and electronic structures at a fundamental level.[19−24]

In such comparisons, it is ideal to examine oxo- and hydroxometal adducts in complexes where the rest of the coordination environment is identical. One of us has reported a pair of manganese(IV) complexes stabilized by the cross-bridged cyclam ligand $Me_2EBC$ ($Me_2EBC$ = 4,11-dimethyl-1,4,6,11-tetraazabicyclo[6.6.2]hexadecane), $[Mn(OH)_2(Me_2EBC)]^{2+}$ (**1**), and $[Mn(O)(OH)(Me_2EBC)]^{+}$ (**2**),[12,25] that differ by only a proton (Scheme 1). These compounds are thus ideally suited for comparing the properties of oxo- and

---

*To whom correspondence should be addressed. E-mail: taj@ku.edu. Phone: (785) 864-3968. Fax: (785) 864-5396.

(1) Costas, M.; Mehn, M. P.; Jensen, M. P.; Que, L., Jr. *Chem. Rev.* **2004**, *104*, 939–986.
(2) Groves, J. T. *J. Inorg. Biochem.* **2006**, 100.
(3) Mukhopadhyay, S.; Mandal, S. K.; Bhaduri, S.; Armstrong, W. H. *Chem. Rev.* **2004**, *104*, 3981–4026.
(4) Stone, K. L.; Borovik, A. S. *Curr. Opin. Chem. Biol.* **2009**, *13*, 114–118.
(5) McGarrigle, E. M.; Gilheany, D. G. *Chem. Rev.* **2005**, *105*, 1565–1602.
(6) Meunier, B.; De Visser, S. P.; Shaik, S. *Chem. Rev.* **2004**, *104*, 3947–3980.
(7) Parsell, T. H.; Behan, R. K.; Green, M. T.; Hendrich, M. P.; Borovik, A. S. *J. Am. Chem. Soc.* **2006**, *128*, 8728–8729.
(8) Gross, Z.; Gray, H. B. *Adv. Synth. Catal.* **2004**, *346*, 165–170.
(9) Kerber, W. D.; Goldberg, D. P. *J. Inorg. Biochem.* **2006**, *100*, 838–857.
(10) Fiedler, A. T.; Que, L., Jr. *Inorg. Chem.* **2009**, *48*, 11038–11047.
(11) Jensen, M. P.; Costas, M.; Ho, R. Y. N.; Kaizer, J.; Mairata i Payeras, A.; Munck, E.; Que, L., Jr.; Rohde, J.-U.; Stubna, A. *J. Am. Chem. Soc.* **2005**, *127*, 10512–10525.
(12) Yin, G.; Danby, A. M.; Kitko, D.; Carter, J. D.; Scheper, W. M.; Busch, D. H. *J. Am. Chem. Soc.* **2007**, *129*, 1512–1513.
(13) Xu, A.; Xiong, H.; Yin, G. *Chem.—Eur. J.* **2009**, *15*, 11478–11481.
(14) Goldsmith, C. R.; Cole, A. P.; Stack, T. D. P. *J. Am. Chem. Soc.* **2005**, *127*, 9904–9912.
(15) Yin, G.; Danby, A. M.; Kitko, D.; Carter, J. D.; Scheper, W. M.; Busch, D. H. *J. Am. Chem. Soc.* **2008**, *130*, 16245–16253.
(16) Su, C.; Sahlin, M.; Oliw, E. H. *J. Biol. Chem.* **2000**, *275*, 18830–18835.
(17) Glickman, M. H.; Klinman, J. P. *Biochemistry* **1995**, *34*, 14077–14092.
(18) Minor, W.; Steczko, J.; Stec, B.; Otwinowski, Z.; Bolin, J. T.; Walter, R.; Axelrod, B. *Biochemistry* **1996**, *35*, 10687–10701.
(19) Michel, C.; Baerends, E. J. *Inorg. Chem.* **2009**, *48*, 3628–3638.
(20) Neese, F. *J. Inorg. Biochem.* **2006**, *100*, 716–726.
(21) Decker, A.; Solomon, E. I. *Angew. Chem., Int. Ed.* **2005**, *44*, 2252–2255.
(22) Gunay, A.; Theopold, K. H. *Chem. Rev.* **2010**, *110*, 1060–1081.
(23) Nam, W. *Acc. Chem. Res.* **2007**, *40*, 522–531.
(24) Shaik, S. *Acc. Chem. Res.* **2007**, *40*, 532–542.
(25) Yin, G.; McCormick, J. M.; Buchalova, M.; Danby, A. M.; Rodgers, K.; Day, V. W.; Smith, K.; Perkins, C. M.; Kitko, D.; Carter, J. D.; Scheper, W. M.; Busch, D. H. *Inorg. Chem.* **2006**, *45*, 8052–8061.

**Scheme 1**

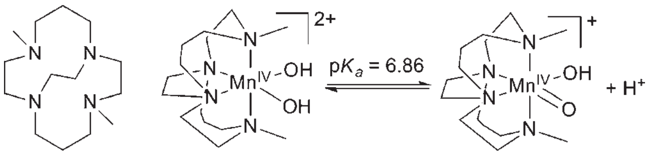

Me$_2$EBC 1 2

hydroxometal adducts. pH titration experiments have shown that **1** converts to **2** with a p$K_a$ of 6.86.[25] The solid-state structure of **1** was determined by X-ray crystallography,[25] and the composition of **2** was established using mass spectrometry.[26] The bond dissociation enthalpies (BDEs) of the respective reduced products of **1** and **2** are similar (BDE = 83 and 84.3 kcal mol$^{-1}$ for the Mn$^{III}$OH$_2$ and Mn$^{III}$OH species).[12]

With regards to the kinetics of the HAT reactions, the Mn$^{IV}$=O species **2** exhibits HAT rates ~14-fold greater than those of **1** when 1,4-cyclohexadiene (CHD), 9,10-dihydroanthracene (DHA), xanthene, and fluorene are used as substrates.[12,15] While the paucity of oxo- and hydroxometal adducts with all other ligands being identical renders it difficult to provide an even comparison for this rate enhancement, it is notable that the rate enhancement observed for **2** is significantly less than that reported for the oxo- and hydroxoiron(IV) adducts of the tetradentate BPMCN ligand [BPMCN = *N*,*N*′-bis(2-pyridylmethyl)-*N*,*N*′-dimethyl-*trans*-1,2-diaminocyclohexane]. In that case, the oxoiron(IV) adduct, [Fe(O)(pyridine)($\beta$-BPMCN)]$^{2+}$, was shown to perform HAT reactions for the organic substrates CHD, DHA, and 2,4,6-tri-*tert*-butylphenol with rates 10$^2$−10$^3$-fold greater than the hydroxoiron(IV) complex [Fe(OH)(OO$^t$Bu)($\beta$-BPMCN)]$^{2+}$.[10−15] Using the framework of frontier molecular orbital (MO) theory, this difference in reactivity was attributed to the large percentage of oxo character in the Fe$^{IV}$=O $\pi$* MOs. Indeed, Solomon and co-workers have used experimental and computational methods to show that increased oxo character in the $\pi$* MOs of Fe$^{IV}$=O compounds correlates with an increase in the HAT rates for a given substrate.[27,28] However, for [Fe(O)(pyridine)($\beta$-BPMCN)]$^{2+}$ and [Fe(OH)(OO$^t$Bu)($\beta$-BPMCN)]$^{2+}$, the change from pyridine to alkylperoxo ligand could influence the HAT reaction rate. The reported reactivities of **1** and **2** provide an even comparison of oxo- versus hydroxometal species; what is currently lacking is an experimentally validated description of the frontier MOs of these complexes.

To develop electronic structure comparisons of oxo- and hydroxometal adducts in identical coordination environments, we have examined **1** and **2** using electronic absorption (Abs) and magnetic circular dichroism (MCD) spectroscopies and density functional theory (DFT) computations. This work provides insights into factors governing the reactivities of high-valent metal complexes and establishes spectral assignments for Mn$^{IV}$OH and Mn$^{IV}$=O centers that could aid in the identification of related intermediates.

## Materials and Methods

**Preparation of [Mn$^{IV}$(OH)$_2$(Me$_2$EBC)](PF$_6$)$_2$ (1) and [Mn$^{IV}$(O)(OH)(Me$_2$EBC)](PF$_6$) (2).** **1** was synthesized by oxidizing [Mn$^{II}$(Me$_2$EBC)Cl$_2$] with H$_2$O$_2$ in the presence of NH$_4$PF$_6$ in H$_2$O.[25] pH titration experiments have furnished an acid−base equilibrium for **1** and **2** with a p$K_a$ of 6.86 in an aqueous solution. Thus, in a weakly acidic solution, **1** is the major species. At pH 8.4, approximately 98% of the sample is present as **2**. A mull MCD sample of **1** was prepared by mixing 15 mg of **1** with 1 mL of poly(dimethylsiloxane) with a mortar and pestle until a uniform mixture was observed. The mixture was then sandwiched between two quartz disks. The two disks were mounted in a sample holder and flash-frozen with liquid nitrogen. The MCD sample for **2** was prepared by dissolving 30 mg of **1** in 15 mL of H$_2$O. The pH was adjusted to 8.4 using 0.1 M NaOH. Water was removed in vacuo. Once dry, a mull sample of **2** was prepared using the procedure described above. Because Abs and electrospray ionization mass spectrometric data collected for **2** before and after solvent removal were indistinguishable (Figure S1 in the Supporting Information), we concluded that this procedure did not affect the composition of **2**.

**Absorption and MCD Instrumentation.** Abs data were collected on a Cary 50 Bio spectrometer (Varian). MCD data were collected on a spectropolarimeter (Jasco J-815) interfaced with an Oxford Instruments SM-4000-8 magnetocryostat.

**Variable-Temperature, Variable-Field (VTVH) MCD Data Analysis and Fitting.** VTVH MCD data collected for **1** at 17 400 and 26 000 cm$^{-1}$ were fitted using the general method developed by Neese and Solomon.[29] Fits were performed for an $S$ = $^3/_2$ system with an isotropic $g$ value of 2.00. Using a previously described protocol,[30] zero-field-splitting (ZFS) parameters $D$ and $E/D$ were systematically varied, while the transition moment products were optimized for a given set of ZFS parameters. For both data sets, excellent fits were observed with $D$ = −1.0 cm$^{-1}$ and $E/D$ = 0.05. The transition polarizations found using these ZFS parameters are as follows: 17 400 cm$^{-1}$ band, 0.5% $x$, 0.5% $y$, and 99% $z$ polarization; 26 000 cm$^{-1}$ band, 2% $x$, 4% $y$, and 94% $z$ polarization.

**DFT Computations.** All calculations were performed using the *ORCA 2.7.0* software package developed by F. Neese (University of Bonn).[31] The crystal structure coordinates of **1** served as a starting point for DFT energy minimizations. The DFT geometry-optimized structure of this complex was used for subsequent calculations so as to provide a reasonable comparison with **2**, for which no X-ray structure is available. Geometry optimizations of **1** and **2** were converged to the $S$ = $^3/_2$ spin state and utilized the Becke−Perdew (BP86) functional[32,33] and the SVP (for C and H) and TZVP (for Mn, N, and O) basis sets.[34,35] Because these calculations employed a resolution of the identity approximation,[36] the SV/J and TZV/J auxiliary basis sets were also used.[34,35]

Electronic transition energies and intensities were computed for **1** and **2** using the time-dependent DFT (TD-DFT) method[37−39]

---

(26) Yin, G.; Buchalova, M.; Danby, A. M.; Perkins, C. M.; Kitko, D.; Carter, J. D.; Scheper, W. M.; Busch, D. H. *J. Am. Chem. Soc.* **2005**, *127*, 17170–17171.

(27) Decker, A.; Rohde, J.-U.; Klinker, E. J.; Wong, S. D.; Que, L., Jr.; Solomon, E. I. *J. Am. Chem. Soc.* **2007**, *129*, 15983–15996.

(28) Solomon, E. I.; Wong, S. D.; Liu, L. V.; Decker, A.; Chow, M. S. *Curr. Opin. Chem. Biol.* **2009**, *13*, 99–113.

(29) Neese, F.; Solomon, E. I. *Inorg. Chem.* **1999**, *38*, 1847–1865.

(30) Jackson, T. A.; Karapetian, A.; Miller, A.-F.; Brunold, T. C. *Biochemistry* **2005**, *44*, 1504–1520.

(31) Neese, F. *ORCA—an ab initio, Density Functional and Semiempirical Program Package*, version 2.7; University of Bonn: Bonn, Germany, 2009.

(32) Becke, A. D. *J. Chem. Phys.* **1986**, *84*, 4524–4529.

(33) Perdew, J. P. *Phys. Rev. B* **1986**, *33*, 8822–8824.

(34) Schäfer, A.; Horn, H.; Ahlrichs, R. *J. Chem. Phys.* **1992**, *97*, 2571–2577.

(35) Schäfer, G.; Huber, C.; Ahlrichs, R. *J. Chem. Phys.* **1994**, *100*, 5829–5835.

(36) Neese, F. *J. Comput. Chem.* **2003**, *24*, 1740–1747.

(37) Bauernschmitt, R.; Ahlrichs, R. *Chem. Phys. Lett.* **1996**, *256*, 454–464.

(38) Casida, E. M.; Jamorski, C.; Casida, K. C.; Salahub, D. R. *J. Chem. Phys.* **1998**, *108*, 4439–4449.

(39) Stratman, R. E.; Scuseria, G. E.; Frisch, M. J. *J. Chem. Phys.* **1998**, *109*, 8218–8224.

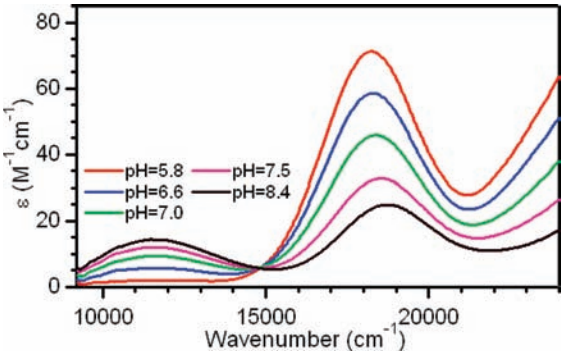

**Figure 1.** 298 K Abs spectra showing the conversion of $[Mn^{IV}(OH)_2(Me_2EBC)]^{2+}$ to $[Mn^{IV}(O)(OH)(Me_2EBC)]^{+}$ as the pH is increased from 5.8 to 8.4.

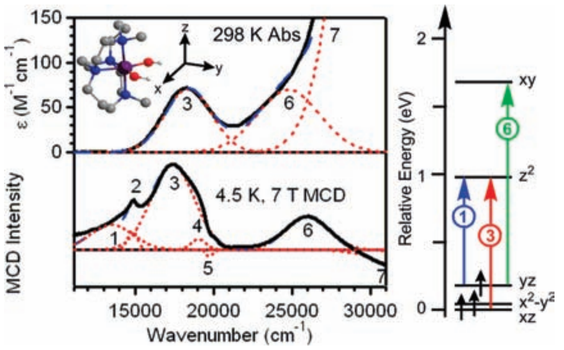

**Figure 2.** Left: Abs spectrum of $[Mn^{IV}(OH)_2(Me_2EBC)]^{2+}$ in $H_2O$ at pH 5.8 (top) and 4 K, 7 T MCD spectrum of a mull sample of **1** (bottom). Individual transitions (red dotted lines) and their sums (blue dashed lines), obtained from an iterative Gaussian fit of the data sets, are displayed on their respective spectra. Inset: Model of **1** developed using DFT computations. The axis system relates to the *D*-tensor orientation obtained from coupled-perturbed DFT computations. Right: Energy-level diagram of $Mn^{IV}$ d-based spin-down MOs from DFT computations and d−d transitions (arrows).

within the Tamm−Dancoff approximation.[40,41] The B3LYP functional[42−44] and SVP (for C and H) and TZVP (for Mn, N, and O) basis sets were employed for these computations. In each calculation, 40 excited states were calculated by including all one-electron excitations within an energy window of ±3 hartree with respect to the energies of the highest occupied and lowest unoccupied MOs. Isosurface plots of MOs were generated using the *gOpenMol* program[45] with isodensity values of 0.05 $b^{-3}$. ZFS parameters and the *D*-tensor orientation were computed for **1** using a linear response method referred to as the coupled-perturbed spin−orbit coupling approach.[46] This calculation utilized the B3LYP functional and TZVP basis sets on all atoms. These calculations yielded $D$ and $E/D$ values of $-1.7$ cm$^{-1}$ and 0.21, respectively, in acceptable agreement with the experimental values determined by analysis of the VTVH MCD data ($D = -1$ cm$^{-1}$ and $E/D = 0.05$).

## Results and Discussion

**Conversion of $[Mn^{IV}(OH)_2(Me_2EBC)]^{2+}$ to $[Mn^{IV}(O)(OH)(Me_2EBC)]^{+}$.** Figure 1 shows the pH-dependent conversion of **1** to **2** as followed by Abs spectroscopy. At pH 5.8, the dominant species is **1**, which displays a single feature at ∼18 200 cm$^{-1}$ (550 nm). As the pH is raised, **1** converts to **2** ($pK_a = 6.86$), and the 18 200 cm$^{-1}$ band loses intensity and blue-shifts slightly. A new, broad feature also appears at ∼11 500 cm$^{-1}$ (870 nm). The formation of **2** is maximized at pH 8.4. The intensities of all near-IR and visible absorption features for **1** and **2** are low (< 100 M$^{-1}$ cm$^{-1}$), and these bands are thus attributed to $Mn^{IV}$ d−d transitions. To develop detailed assignments for these electronic transitions, we used MCD spectroscopy, a very sensitive probe of metal-centered d−d transitions.[29,47]

**Spectroscopic Data and Analysis for $[Mn^{IV}(OH)_2(Me_2EBC)]^{2+}$.** The 4 K, 7 T mull MCD spectrum of **1** (Figure 2) displays two prominent, positive features at ∼17 000 and 26 000 cm$^{-1}$ (bands 3 and 6, respectively). A negative band is observed above 30 000 cm$^{-1}$, which is likely due to charge-transfer (CT) transitions. Additional fine structure is resolved at ∼14 900 and 20 000 cm$^{-1}$ (bands 2, 4, and 5). All features are temperature-dependent *C*-term signals (Figure S2 in the Supporting Information) attributed to paramagnetic **1**. An iterative Gaussian deconvolution of the Abs and MCD spectra of **1** reveals seven electronic transitions below 31 000 cm$^{-1}$ (Table S1 in the Supporting Information).[48] The different selection rules of Abs and MCD spectroscopy permit general band assignments to be made by comparing Abs and MCD intensities. For example, while metal-centered d−d transitions are parity-forbidden and thus weak in an Abs spectrum, these transitions are selectively enhanced in the MCD spectrum. In contrast, CT bands that dominate Abs spectra are comparatively weaker in MCD spectra. On the basis of these general rules, bands 1, 3, and 6, which are prominent in the MCD spectrum but correspond to weaker Abs features, are assigned as spin-allowed $Mn^{IV}$ d−d transitions. Band 7, which carries a significant absorption intensity but is fairly weak in the MCD spectrum, is assigned as a CT band, likely hydroxo-to-manganese(IV) in origin. Bands 2, 4, and 5, which have narrow bandwidths and negligible absorption intensities, are attributed to spin-forbidden $Mn^{IV}$ d−d transitions.

The polarizations of bands 3 and 6, as well as the ground-state ZFS parameters of **1**, were examined using VTVH MCD spectroscopy. In this technique, the intensity of an MCD band is monitored as a function of the magnetic field at various fixed temperatures. Transition polarizations obtained through fitting of these data provide important information for the development of detailed spectral assignments (vide infra). VTVH MCD curves for bands 3 and 6 are similar in appearance, and both are well-fit with $D = -1$ cm$^{-1}$, $E/D = 0.05$, and a predominant *z* polarization (Figure 3). The ZFS parameters fall within the range of values observed for $Mn^{IV}$ centers.[7,49,50]

DFT and TD-DFT computations were performed to further analyze the electronic structure of **1**. A geometry-optimized model of **1**, based on the X-ray coordinates,

---

(40) Hirata, S.; Head-Gordon, M. *Chem. Phys. Lett.* **1999**, *302*, 375–382.
(41) Hirata, S.; Head-Gordon, M. *Chem. Phys. Lett.* **1999**, *314*, 291–299.
(42) Becke, A. D. *J. Chem. Phys.* **1993**, *98*, 1372–1377.
(43) Becke, A. D. *J. Chem. Phys.* **1993**, *98*, 5648–5652.
(44) Lee, C.; Yang, W.; Parr, R. G. *Phys. Rev. B* **1988**, *37*, 785–789.
(45) Laaksonen, L. *J. Mol. Graphics* **1992**, *10*, 33–34.
(46) Neese, F. *J. Chem. Phys.* **2007**, *127*, 164112–164119.
(47) Kirk, M. L.; Peariso, K. *Curr. Opin. Chem. Biol.* **2003**, *7*, 220–227.

(48) The energies of the Gaussian bands in the Abs and MCD fits were allowed to vary by ∼5% to account for experimental band shifts upon going from 298 to 4 K.

(49) Min, K. S.; Weyermuller, T.; Wieghardt, K. *Dalton Trans.* **2004**, 178–186.

(50) Duboc, C.; Collomb, M.-N. *Chem. Commun.* **2009**, 2715–2717.

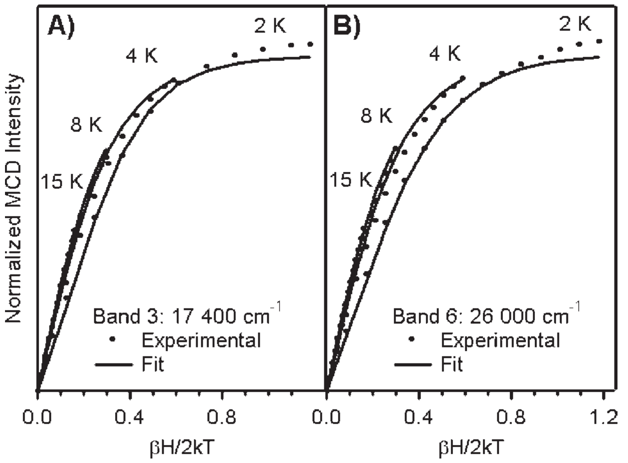

**Figure 3.** VTVH MCD data for $[Mn^{IV}(OH)_2(Me_2EBC)]^{2+}$ collected at 17 400 (A) and 26 000 (B) $cm^{-1}$ (dotted lines) and best fits (solid lines) to these data. Both data sets were fit with $D = -1\ cm^{-1}$ and $E/D = 0.05$. Transition polarizations used for these fits are as follows: (A) 17 400 $cm^{-1}$ (band 3), 0.5% $x$, 0.5% $y$, and 99% $z$ polarization; (B) 26 000 $cm^{-1}$ (band 6), 2% $x$, 4% $y$, and 94% $z$ polarization.

**Table 1.** Manganese−Ligand Bond Lengths for $[Mn^{IV}(OH)_2(Me_2EBC)]^{2+}$ and $[Mn^{IV}(O)(OH)(Me_2EBC)]^{+}$ Obtained from X-ray Diffraction (XRD) and DFT Computations

| | **1**(XRD)[a] | **1**(DFT) | **2**(DFT) |
|---|---|---|---|
| Mn−O(H)[b] | 1.811 | 1.814 | 1.682 |
| Mn−OH | 1.811 | 1.814 | 1.838 |
| $Mn-N^{Me}$ | 2.110 | 2.205 | 2.156 |
| $Mn-N^{Me}$ | 2.110 | 2.205 | 2.150 |
| Mn−N | 2.090 | 2.139 | 2.261 |
| Mn−N | 2.090 | 2.139 | 2.184 |

[a] Metric parameters obtained from ref 25. [b] This Mn−O distance refers to the Mn−OH and Mn=O distances for **1** and **2**, respectively.

was used for our analysis of the electronic structure to afford a comparison with **2**, for which no X-ray data are available. The optimized structure of **1** displays manganese−ligand bond lengths very similar to those observed in the X-ray structure (Table 1). While the computed Mn−OH bond lengths are within 0.003 Å of those observed experimentally, the Mn−N bond lengths are overestimated by up to 0.095 Å. This is consistent with the general observation that DFT calculations for transition-metal complexes provide more reliable distances for shorter, stronger metal−ligand bonds than for longer, weaker bonds.[51] Because the electronic properties of **1** are dominated by the $Mn^{IV}-OH$ interactions, the discrepancy in the Mn−N distances is not expected to negatively affect our analysis.

To relate the transition polarizations obtained by VTVH MCD spectroscopy with the DFT-derived structure of **1**, we used a coordinate system defined by the $D$ tensor obtained from coupled-perturbed DFT computations (Figure 2),[46,52] where the $y$ axis bisects the Mn−OH bonds and the $z$ axis lies along the $N^{Me}-Mn-N^{Me}$ vector.[53] The computed $Mn^{IV}$ d orbital splitting indicates a large distortion from octahedral symmetry owing to the different ligand-field strengths of the amine and $OH^-$ ligands (Figure 2). The empty $e_g$-derived MOs ($z^2$ and $xy$) are split considerably, with the $xy$ MO at higher energy. This MO is strongly Mn−OH σ-antibonding with 24% $OH^-$ character (Table S2 in the Supporting Information). All singly occupied $t_{2g}$-derived orbitals ($xz$, $x^2-y^2$, and $yz$) are weakly Mn−OH π-antibonding, with the $yz$ MO highest in energy.

Because **1** is an $S = {}^3/_2$ $d^3$ system with approximate $C_{2v}$ symmetry, six spin-allowed d−d transitions are expected. The appearance of only three d−d bands in the Abs and MCD spectra of **1** (Figure 2) suggests that some transitions occur at energies greater than 30 000 $cm^{-1}$ and/or are obscured by CT bands. The three d−d transitions observed for **1** can be assigned using transition polarization information from VTVH MCD data and TD-DFT computations. These assignments are summarized in Table 2. Band 1, which displays no absorption intensity (Figure 2), is assigned as the electric-dipole-forbidden $yz \rightarrow z^2$ transition, which likely gains MCD intensity through spin−orbit coupling. This assignment is corroborated by TD-DFT computations that predict this transition at 16 750 $cm^{-1}$, in good agreement with the experimental energy of band 1 (14 500 $cm^{-1}$). VTVH MCD data collected for bands 3 and 6 (Figure 3) indicate that both transitions are $z$-polarized, which, according to a group theory analysis (see Supporting Information), permits their assignments as the $xz \rightarrow z^2$ and $yz \rightarrow xy$ transitions. TD-DFT computations predict the $xz \rightarrow z^2$ transition at lower energy (18 200 $cm^{-1}$), in good agreement with band 3 (17 400 $cm^{-1}$). Band 6 is thus assigned as the $yz \rightarrow xy$ transition (Table 2).

Although only three d−d bands are resolved for **1**, their transition energies provide important insights into bonding. For example, the large energy difference between the $yz \rightarrow z^2$ and $yz \rightarrow xy$ transitions is an indicator of the splitting of the $e_g$-derived $z^2$ and $xy$ MOs (Figure 2) and thus reflects the relative strengths of the $Mn^{IV}-N_{amine}$ and $Mn^{IV}-OH$ interactions. Similarly, the difference in energy between the $yz \rightarrow xy$ and $xz \rightarrow xy$ transitions provides insights into $Mn^{IV}-OH$ π interactions. Determining how these splittings are perturbed for **2** will afford a comparison of σ and π interactions in these complexes.

**Spectroscopic Data and Analysis for $[Mn^{IV}(O)(OH)(Me_2EBC)]^+$.** The 4 K, 7 T MCD spectrum of **2** reveals a series of positively signed features from 10 000 to 31 000 $cm^{-1}$ (Figure 4). Variable-temperature MCD data collected for **2** (Figure S3 in the Supporting Information) show all features to be $C$ term in origin. An iterative Gaussian deconvolution of the Abs and MCD spectra of **2** (Figure 4) reveals seven electronic transitions below 31 000 $cm^{-1}$ that can be qualitatively assigned on the basis of their Abs and MCD intensities. Bands 1, 2, and 4−6 are assigned as spin-allowed d−d transitions, whereas the narrower and less intense band 3 is attributed to a spin-forbidden d−d transition. Band 7 corresponds to an intense Abs feature and is therefore attributed to a CT transition.

Metric parameters for a geometry-optimized model of **2** are collected in Table 1. The Mn=O distance of 1.682 Å is significantly shorter than the Mn−OH distance

---

(51) Neese, F. *J. Biol. Inorg. Chem.* **2006**, *11*, 702–711.

(52) Scheifele, Q.; Riplinger, C.; Neese, F.; Weihe, H.; Barra, A.-L.; Juranyi, F.; Podlesnyak, A.; Tregenna-Piggott, P. L. W. *Inorg. Chem.* **2007**, *47*, 439–447.

(53) The $D$-tensor coordinate system of **1** is related to the canonical $C_{2v}$ point group coordinate system (i.e., where the $z$ axis is coincident with the $C_2$ axis) by an interchange of the $z$ and $y$ axes.

**Table 2.** Electronic Transition Energies ($cm^{-1}$) Obtained from a Gaussian Analysis of Abs and MCD Spectra of **1** and **2** and TD-DFT Computations

| | $[Mn^{IV}(OH)_2(Me_2EBC)]^{2+}$ | | | $[Mn^{IV}(O)(OH)(Me_2EBC)]^{+}$ | | |
|---|---|---|---|---|---|---|
| transition | band | expt | TD-DFT[a] | band | expt | TD-DFT[a] |
| $yz \rightarrow z^2$ (forbidden)[b] | 1 | 14 500 | 16 750 | 2 | 13 700 | 12 500 |
| $xz \rightarrow z^2$ ($z$-polarized)[b] | 3 | 17 400 ($z$)[a] | 18 200 | 4 | 18 000 | 18 200 |
| $yz \rightarrow xy$ ($z$-polarized)[b] | 6 | 26 000 ($z$)[a] | 23 000 | 6 | 24 000 | 21 050 |
| $x^2$-$y^2 \rightarrow z^2$ ($y$-polarized)[b] | ND | | 24 900 | 1 | 11 600 | 12 100 |
| $x^2$-$y^2 \rightarrow xy$ ($x$-polarized)[b] | ND | | 28 200 | 5 | 21 000 | 19 550 |

[a] Transition polarizations from VTVH MCD data collected for **1**. [b] Transition polarization predicted by group theory analysis for **1** using $C_{2v}$ symmetry and the $D$-tensor coordinates (Figure 2).

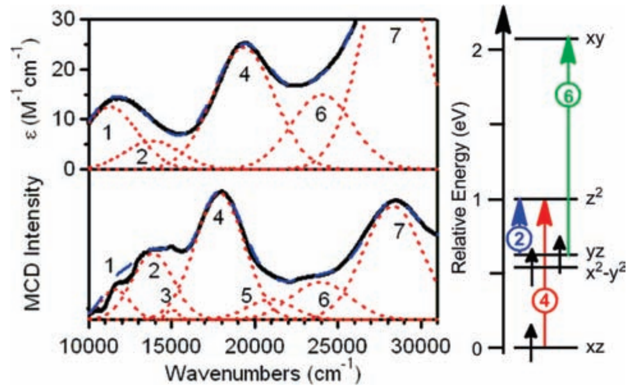

**Figure 4.** Left: Abs spectrum of $[Mn^{IV}(O)(OH)(Me_2EBC)]^+$ in $H_2O$ at pH 8.4 (top) and 4 K, 7 T MCD spectrum of a mull sample of **2** (bottom). Individual transitions (red dotted lines) and their sums (blue dashed lines), obtained from an iterative Gaussian fit of the data sets, are displayed on their respective spectra. Right: Energy-level diagram of the $Mn^{IV}$ d-based spin-down MOs of **2** from DFT computations and d−d transitions.

(1.838 Å), indicative of the expected Mn=O double-bond character. To develop spectral assignments for the d−d bands of **2**, TD-DFT computations were performed. A comparison of the experimental and computed Abs spectra of **2** is shown in Figure 5. TD-DFT computations predict two d−d transitions ($x^2-y^2 \rightarrow z^2$ and $yz \rightarrow z^2$) to give rise to a feature at ~12 000 $cm^{-1}$, in good agreement with the near-IR feature of **2** that is composed of bands 1 and 2 (Table 2 and Figure 5). Using the same coordinate system that was used for **1**, the $x^2-y^2$ and $yz$ MOs of **2** are the $Mn^{IV}$=O $\pi^*$ MOs that carry significant (~25%) oxo character. The low energies of the $x^2-y^2 \rightarrow z^2$ and $yz \rightarrow z^2$ transitions for **2** (11 600 and 13 700 $cm^{-1}$, respectively) reflects the strong $\pi$-donating abilities of the oxo ligand. This parallels that observed for $Fe^{IV}$=O complexes, which also exhibit near-IR features indicative of strong Fe=O $\pi$ interactions.[27,54] The TD-DFT computations predict a moderately intense $xz \rightarrow z^2$ transition at ~18 200 $cm^{-1}$ that corresponds well with band 4 (Figure 5). The $x^2-y^2 \rightarrow xy$ and $yz \rightarrow xy$ transitions are predicted at slightly higher energy and with significantly lower absorption intensities. The experimentally observed bands 5 and 6 (Figures 4 and 5) are respectively attributed to these transitions. These assignments are summarized in Table 2.

**Comparison of $[Mn^{IV}(OH)_2(Me_2EBC)]^{2+}$ and $[Mn^{IV}(O)(OH)(Me_2EBC)]^{2+}$.** For both **1** and **2**, the difference between the $yz \rightarrow z^2$ and $yz \rightarrow xy$ transition energies provides a direct probe of the splitting of the $e_g$-derived acceptor orbitals in these complexes and thus offers a comparison of $\sigma$ interactions. The experimental transition energies reveal that **1** has a larger splitting of the $e_g$-derived orbitals by ~1000 $cm^{-1}$ (Table 2), which might initially appear surprising given the short Mn=O bond length in **2** and the comparable Mn−OH and Mn−N bond lengths of **1** and **2** (Table 1). DFT computations suggest that this result can be attributed to destabilization of the $z^2$ MO of **2** due to an admixture of the hydroxide character (Table S3 in the Supporting Information). Overall, DFT computations predict $Mn^{IV}$−O(H) $\sigma$ interactions to be similar for these complexes, with 25 and 30% oxo/hydroxo character in the $xy$ MOs of **1** and **2**, respectively (Figure 6). In contrast, DFT computations predict the ligand character in the $yz$ MO to nearly double when the oxo ligand is present (Figure 6). Experimentally, this is reflected in the larger splitting of the $yz \rightarrow z^2$ and $xz \rightarrow z^2$ transitions for **2** and the low energy of the $x^2-y^2 \rightarrow z^2$ transition (Table 2). We note that a similar doubling of the ligand character of the $\pi^*$ MOs was predicted for the oxoiron(IV) $[Fe(O)(pyridine)(\beta\text{-BPMCN})]^{2+}$ complex relative to the hydroxoiron(IV) compound $[Fe(OH)(OO^tBu)(\beta\text{-BPMCN})]^{2+}$.[10]

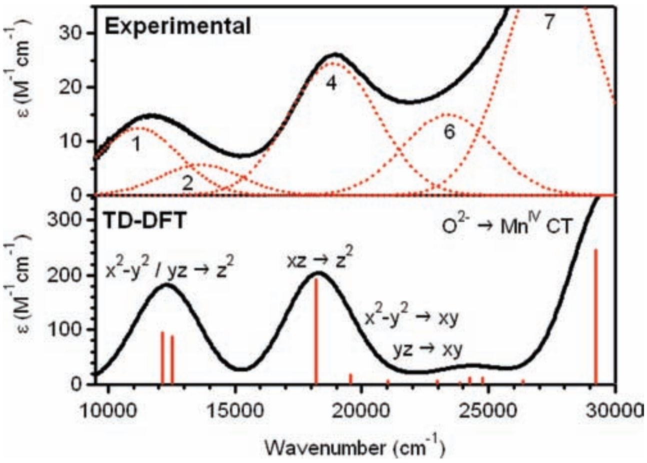

**Figure 5.** Top: Experimental absorption spectrum of $[Mn^{IV}(O)(OH)(MeEBC)]^+$ at 298 K (solid line) and the corresponding Gaussian deconvolution (dotted lines). Bottom: Simulated absorption spectrum based on TD-DFT computations for **2**. Individual electronic transitions are indicated by vertical sticks, and key features are labeled. Complete results of the TD-DFT computations for **2** are provided in Table S5 in the Supporting Information.

The significant difference in $\pi$ interactions between **1** and **2** might initially appear at odds with the small rate enhancement for HAT reactions (~14-fold), because according to the frontier MO theory, the percentage of ligand character in the frontier MOs is expected to correlate with the rate of HAT.[27,28] This is especially

---

(54) Decker, A.; Rohde, J.-U.; Que, L., Jr.; Solomon, E. I. *J. Am. Chem. Soc.* **2004**, *126*, 5378–5379.

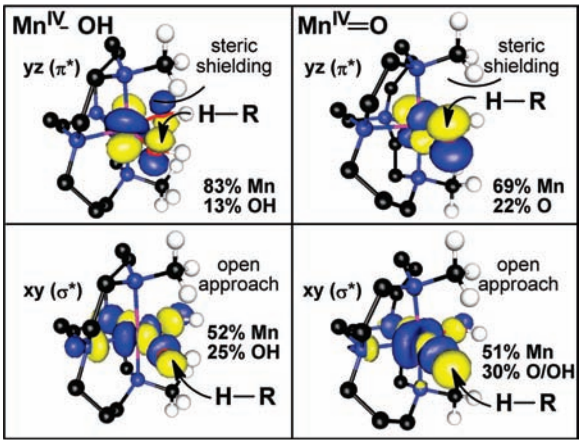

**Figure 6.** Surface contour plots of the $\text{Mn}^{IV}$ *yz* and *xy* MOs of **1** (left) and **2** (right). Routes for substrate approaches are indicated with arrows.

apparent when compared with the $[\text{Fe(O)(pyridine)}(\beta\text{-BPMCN})]^{2+}$ and $[\text{Fe(OH)(OO}^t\text{Bu)}(\beta\text{-BPMCN})]^{2+}$ compounds, where rate enhancements of $10^2-10^3$-fold were observed.[10] One possible explanation for the more dramatic changes in the HAT rates for the iron(IV) complexes could be the difference in the sixth ligand (alkylperoxo for $\text{Fe}^{IV}\text{OH}$ and pyridine for $\text{Fe}^{IV}{=}\text{O}$), whereas the only difference between **1** and **2** is a proton.

An alternative explanation relates to the steric properties of the $\text{Me}_2\text{EBC}$ ligand. For HAT reactions of Fe and Mn centers, both the $\pi^*(\beta)$ and $\sigma^*(\alpha)$ LUMOs can serve as the redox-active orbitals.[19,28] However, to maximize orbital overlap between the substrate and redox-active MO, reactions proceeding by the $\pi^*(\beta)$ MOs will require the substrate C−H bond to be perpendicular to the M=O(H) axis (horizontal approach), whereas the substrate will approach the $\sigma^*(\alpha)$ MO along the M−O(H) axis (vertical approach). Under these considerations, we propose that the $\text{Me}_2\text{EBC}$ ligand prevents substrate interaction with the $\pi^*(\beta)$ LUMOs of **1** and **2**. Inspection of these MOs (Figure 6) reveals that the $\text{Me}_2\text{EBC}$ macrocycle provides steric shielding,[55] hindering the horizontal approach of the substrate.[56] Alternatively, the $\sigma^*(\alpha)$ LUMOs of **1** and **2**, which contain oxo/hydroxo character along the Mn−O(H) bond axis and away from the $\text{Me}_2\text{EBC}$ ligand (Figure 6), could likely offer a lower-energy route for HAT. According to this model, the moderate rate enhancement of **2** relative to **1** would thus be explained by the 5% increase in the oxo/hydroxo character in the $\sigma^*(\alpha)$ LUMO of **2**.

The role of the ligand structure in controlling reaction pathways is important for related protein systems that selectively oxidize substrates by HAT mechanisms. In those cases, the orientation of the substrate is presumably optimized to facilitate proper interaction between the target R−H bond and the appropriate metal−oxo/hydroxo orbital. Optimization of such interactions in synthetic systems could lead to more reactive and selective oxidants and thus should be considered in the design of small-molecule catalysts.

**Acknowledgment.** T.A.J. thanks the University of Kansas for financial support. The authors thank the Proctor and Gamble Co. for samples of the manganese(II) complex used in these studies.

**Supporting Information Available:** Details of transition polarization analysis for **1**, variable-temperature MCD data for **1** and **2**, and the results of DFT and TD-DFT computations for **1** and **2**. This material is available free of charge via the Internet at http://pubs.acs.org.

---

(55) The other $\text{Mn}^{IV}{=}\text{O}$ $\pi^*$ MO for **2** ($x^2-y^2$) is shielded by the backbone of the $\text{Me}_2\text{EBC}$ ligand (Figure S4 in the Supporting Information).

(56) While the orientation of the *yz* MO appears ideally suited for HAT reaction with the methyl groups of the $\text{Me}_2\text{EBC}$ macrocycle, the low BDEs of the corresponding $\text{Mn}^{III}\text{OH}$ and $\text{Mn}^{III}\text{OH}_2$ complexes presumably render such reactions thermodynamically unfavorable.